

Machine vision recognition of weld pool in gas tungsten arc welding

R Kovacevic, PhD, SMSME, MemASME, MAWS and **Y M Zhang**, PhD, MemASME, MAWS
 Center for Robotics and Manufacturing Systems, Department of Mechanical Engineering, University of Kentucky, Lexington, Kentucky, USA

The weld pool and its surrounding area can provide a human welder with sufficient visual information to control welding quality. Seam tracking error and pool geometry can be recognized by a skilled human welder and then utilized to adjust the welding parameters. However, for machine vision, accurate real-time recognition of weld pool geometry is a difficult task due to the high intensity arc light, even though seam tracking errors can be detected. A novel vision system is, therefore, used to acquire quality images against the arc. A real-time recognition algorithm is proposed to analyse the image and recognize the pool geometry based on the pattern recognition technique. Despite surface impurity and other influences, the pool geometry can always be recognized with sufficient accuracy in 150 ms under different welding conditions. To explore the potential application of machine vision in weld penetration control, experiments are conducted to show the correlation between pool geometry and weld penetration state. Thus, pool recognition also provides a possible technique for front-face sensing of the weld penetration.

NOTATION

C_k ($k = 1, \dots, 4$)	k th piece of pool edge
d_{eu}	edge slope
d_0	threshold of edge slope for segmenting
$e_0(j)$ ($j = 1, \dots, K$)	rough pool edge segments
$e_1(j)$ ($j = 1, \dots, K$)	alternative segments
$E^{(i)}$ ($i = 1, \dots, N$)	possible selections for pool edge
$E^{(i^*)}$	selected pool edge
$E^{(i)}(k)$ [$i = 1, \dots, N(k)$]	possible selections for C_k
$E^{(i^*)}(k)$	selected C_k
$f(l)$	second-order derivative of pool edge
\bar{f}_k	mean of $f(l)$ in C_k range
$\bar{f}_{s_j}(j)$ ($s_j = 1, 2$)	mean of $f(l)$ for interior points in segment j , $s_j = 0$ for $e_0(j)$, $s_j = 1$ for $e_1(j)$
$g_{low}(y)$	lowest greyness encountered during scanning along the x -axis direction
J	cost function for recognition
J_k	cost function for recognizing C_k
K_1	number of short segments
$K_1(k)$	number of short segments in C_k range
l_{j0} (l_{j1})	sequential number of initial (ending) point in segment j
$L(j)$	sample size of segment j
L_k	sample size in C_k range
N_{k0} (N_{k1})	sequential number of initial (ending) segment in C_k range
pixel _x	sensor resolution along x direction
pixel _y	sensor resolution along y direction

$T(y)$	threshold for edge detection
$(x_{eu}(y), y)$	upper rough pool edge
$(x_{el}(y), y)$	lower rough pool edge
(x_{iu}, y_i)	initial point for upper rough pool edge search
(x_{il}, y_i)	initial point for lower rough pool edge search
$[y_{i0}, y_{i1}]$	short segment range
$[Y_1, Y_2]$	range of the rough pool edge
$[Y_1^*, Y_2^*]$	range for searching the alternative of pool rear
$Y_{1u}, Y_{2u}, Y_{1l}, Y_{2l}$	boundaries for C_k 's
σ_k^2	variance of $f(l)$ in C_k range
$\sigma_{s_j}^2(j)$ ($s_j = 1, 2$)	variance of $f(l)$ for interior points in segment j , $s_j = 0$ for $e_0(j)$, $s_j = 1$ for $e_1(j)$

1 INTRODUCTION

Skilled welders control the weld quality by adjusting the welding parameters, for example the electrode feeding, moving, weaving and angle, etc., based on their viewing of the weld pool and its surrounding area. Of the welding process information that is extracted, the pool geometry and seam tracking error may be the most crucial. The importance of seam tracking in determining welding quality is well known. The pool geometry may also offer abundant information about the welding quality. To confirm this, experiments have been conducted to explore the potential correlation between pool geometry and weld penetration. It is observed that when weld penetration increases, the sharpness of the weld pool rear increases. This suggests that the pool geometry, associated with the seam tracking information, should be extracted to control the weld quality. Since the seam tracking has been matured, this study will focus on the real-time recognition of weld pool geometry.

Pool oscillation, ultrasonic technique, infrared sensing and radiography have been proposed to sense

The MS was received on 17 August 1993 and was accepted for publication on 21 June 1994.

the pool geometry or size. They are considered indirect methods. The pool oscillation is intended to measure the mass of the weld pool which can be considered as an average description of the weld pool size, rather than the geometry or shape of the weld pool. The ultrasonic sensors must be in close contact with the weldment surface. Its application is therefore restricted. The infrared sensing can acquire the weld pool boundary based on the emissivity change between the solid material and molten metal liquid (1). However, human identification of the weld pool boundary is not easy. This makes it difficult to verify the acquired pool boundary using the recorded infrared images. In the radiographic sensing, the projected X-ray decays when it penetrates the material. The intensity of the received X-ray varies with the penetrated material thickness (2). Thus, the boundary of the deformed weld pool may be detected by the intensity change. In most cases, the thickness change caused by the deformation is very small compared with the weldment thickness. The accuracy of the pool boundary detection will be affected. Also, the application of X-ray to real-time control of the welding process may be difficult because of the required protection.

The vision method can be regarded as a direct one. Among existing vision techniques, the coaxial viewing proposed by Richardson *et al.* (3) has been regarded as a promising approach. Since the weld pool surface is mirror-like, the diffuse reflection of the arc light from the weld pool is weaker than that from the surrounding area. This intensity difference may be used to detect the pool edge. However, the radiation from the pool causes the intensity contrast of the pool against the surrounding area to be low. Also, the surface veins caused by the cooling behind the pool generate frequent intensity changes (4). Some of these veins are concentric with the pool edge. Consequently, rapid detection of the pool edge is difficult (4). Even though an excellent processing algorithm has been developed, it still requires 6.5 seconds to process a frame of image for extracting the pool edge using a VAX 11/785 computer (4). Pietrzak and Packer (5) developed a real-time proportional integral differential (PID) control system of 8 Hz to detect and control the pool width; however, the image processing algorithm failed when oxides or impurities were present.

In this study, an ultra-high shutter speed camera with pulsed-laser illumination has been used to improve the contrast. [This camera was developed by Control Vision Inc. and has been used to sense high-speed, high-temperature processes (6). However, no real-time algorithms have been developed to recognize the weld pools from the sensed images.] Owing to the short duration of the laser pulse, the laser intensity is much greater than the arc intensity and radiation of the weld pool. Also, the pool surface is mirror-like. Thus the laser is not diffusely reflected from the pool as it is from the unmolten material. A well-contrasted weld pool can be sensed, and quality images can be acquired and processed to detect the weld pool edge rapidly and reliably. Under ideal circumstances, a simple algorithm can be employed to extract the edge in only 50 ms. If oxides exist on the pool surface, the projected laser will also be diffusely reflected from the oxide floats as well as from the solid area. Furthermore, an unclean surface may influence the reflection from the solid material. Regard-

less of these imperfect conditions, the pool edge can always be recognized within 150 ms by the image processing and pattern recognition techniques proposed in this paper.

In the next section, the experiments which show the existence of a correlation between the pool geometry and the weld penetration are discussed. Then the vision system is described in Section 3. In Section 4, the performance requirements are determined. An image processing technique is proposed in Section 5 to prepare the possible pool edge candidates. In Section 6, these candidates are then evaluated to extract the pool edge by the proposed pattern recognition technique. In Section 7, the conclusions are presented.

2 PRELIMINARY OBSERVATION

Weld penetration sensing and control with a front-face sensor have been fundamental problems in automated welding. Several ideas have been proposed to sense the weld penetration from the front face (7). Among these possible approaches, the pool oscillation method (8–13) and the structured-light three-dimensional vision method (7, 14) have been implemented in closed-loop control systems. Pool oscillation-based methods can distinguish the partial penetration from the full penetration mode and then maintain the full penetration mode, utilizing the frequency drop associated with the mode transfer from partial to full penetration (11–13). For the structured-light three-dimensional vision approach (7, 14), a precision control of the back-face bead width has been achieved. The weld geometry behind the pool is measured to obtain the weld penetration feedback. In this case, a measure delay exists. To overcome this delay, a complicated advanced control algorithm has been used (14). If the pool geometry can be utilized, the delay will be eliminated. A precision control of weld penetration may be acquired only through a simple control algorithm.

To show the potential correlation between the pool geometry and weld penetration, experiments have been conducted using the d.c. gas tungsten arc welding (GTAW). The material is stainless steel. The power supply is computer controlled and can operate in the range from 10 to 200 A. The arc length, torch trajectory and travel speed can be preprogrammed. The camera views the pool area as it is shown in Fig. 1. The details of the vision system and image processing will be discussed in the following sections. In the experiments, the current varies while the other welding parameters are kept constant. Bead-on-plate welding is conducted on 3 mm thick plates. The argon flowrate is always 10 l/min.

Figure 2 shows the weldment produced by gradually increasing the current while the arc length (3.5 mm) and torch velocity (2 mm/s) are kept constant. Four images of weld pools corresponding to different currents, that is $i = 105, 110, 113$ and 118 A are given in Fig. 3. It is observed that the weld pool shape characteristic varies gradually with the current during the welding. At the beginning, the pool looks like an ellipse. The front and rear of the pool have little difference in shape. However, as weld penetration increases (that is the depth of penetration increases in the partial mode, the penetration mode transfers from the partial to full penetration mode or the back-face bead width increases in the full pen-

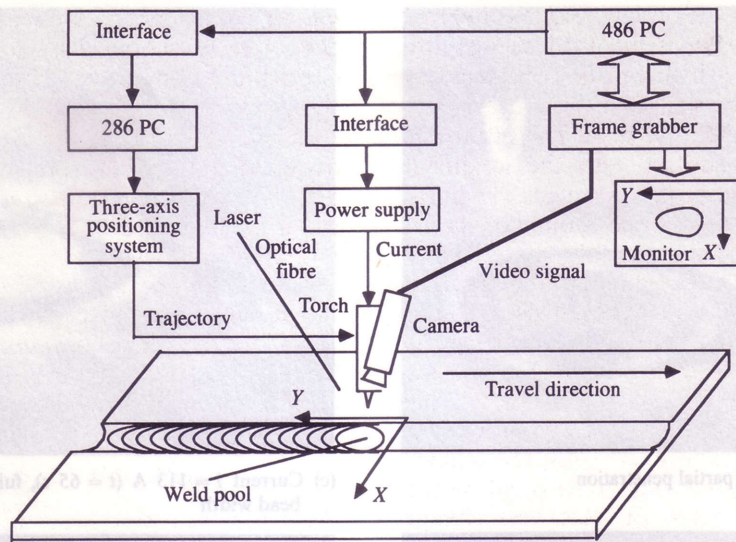


Fig. 1 Experimental set-up

etration mode), the shape of the weld pool begins to differ. While the front shape remains almost unchanged, the rear becomes sharp. This shape change trend can be seen throughout the entire process, that is from shallow to deep to full penetration and from smaller to larger back-face bead width. For example, in Fig. 3a, the weld pool is partially penetrated. In this case, the front and rear shapes are similar. However, in Fig. 3b, the mode has been transferred from the partial penetration to the full penetration. The back-face bead width is 1.9 mm. A sharper weld pool rear is observed. In Fig. 3c and d, the back-face bead widths are 2.9 and 4.5 mm respectively. The corresponding rear shape becomes even sharper than in Fig. 3b. A similar shape change trend is also

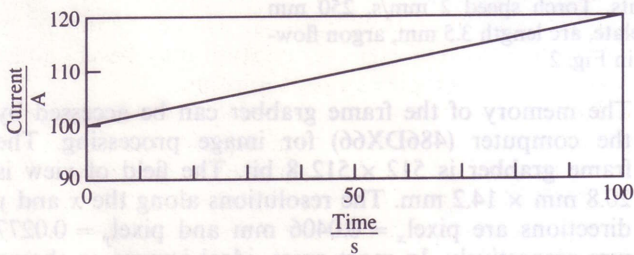
observed in another experiment where all the experimental conditions are the same as already used, except for the arc length which is reduced to 1.2 mm.

In the 3.5 mm arc length experiment, the increase of the front bead width with the current is not significant (see the front-face photograph in Fig. 2). This has also been observed in the 1.2 mm arc length case. However, the weld penetration increases with the current nearly linearly (see the back-face picture in Fig. 2). This implies that the front-face bead width is insensitive to the weld penetration. [A similar conclusion has also been acquired in a previous study (15).] Thus, even though some relationship exists between the weld penetration and pool geometry, the pool geometry cannot accurately be represented solely by the pool width. More geometrical information of the weld pool is required. Hence, precise measurement techniques should be addressed for the pool geometry.

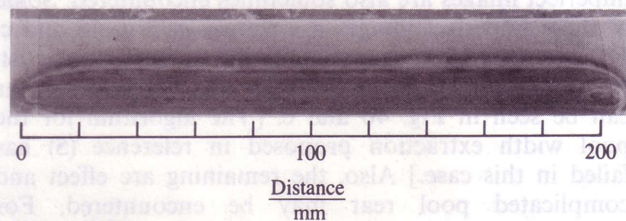
Note that this section is only intended to confirm the possible correlation of the weld pool geometry with the weld quality. If the exact relationship is pursued, additional experiments must be performed under different welding conditions. The inherent characteristic of the pool shape must be found. However, this is beyond the scope of the present study which aims at machine emulation of human vision during welding.

3 VISION SYSTEM

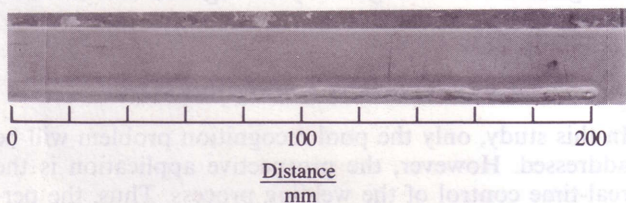
The mirror-like reflectivity of the weld pool tends to eliminate the diffusion reflection of arc light from the pool surface. However, the pool radiation still exists. If the radiation and arc reflection from the solid (unmolten and solidified) material are not much stronger than the radiation from the pool, the weld pool in the resultant images will not be well contrasted against the surrounding area and the recognition of the pool edge will be difficult. Good contrast is needed between the weld pool and surrounding area. In this study, the contrast will be improved by increasing the reflection from the solid area. To do this, a strong illumination must be projected on to the area of interest. The LaserStrobe vision system of the Control Vision Inc. is ideal for this application.



(a) Current



(b) Front-side weld view



(c) Back-side weld view

Fig. 2 Experiment under gradually increasing current

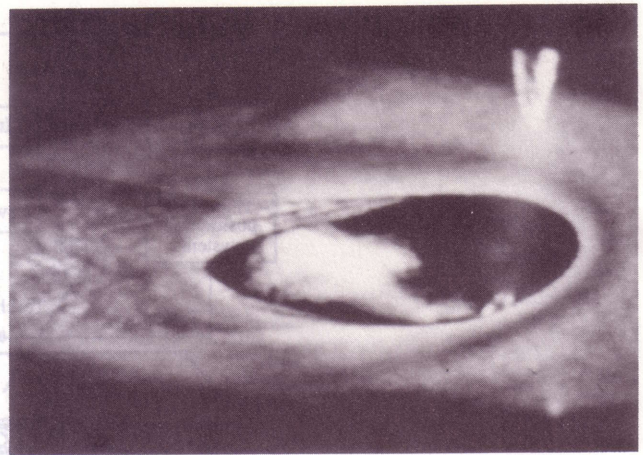
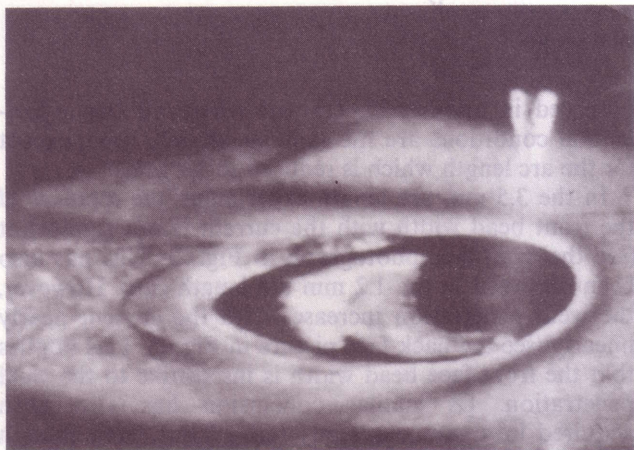
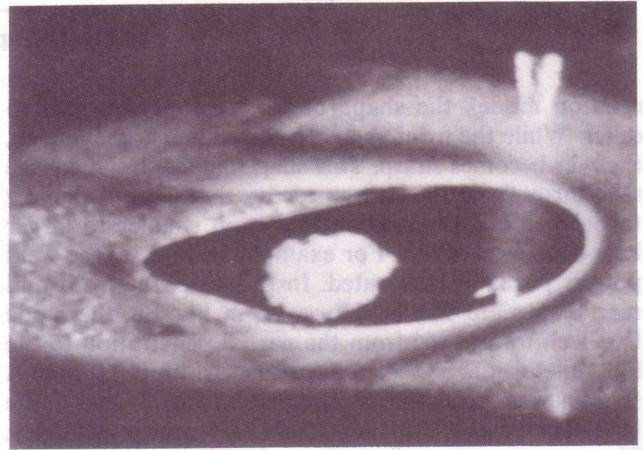
(a) Current $i = 105$ A ($t = 25$ s), partial penetration(c) Current $i = 113$ A ($t = 65$ s), full penetration, 2.9 mm back-face bead width(b) Current $i = 110$ A ($t = 50$ s), full penetration, 1.9 mm back-face bead width(d) Current $i = 118$ A ($t = 90$ s), full penetration, 4.5 mm back-face bead width

Fig. 3 Weld pools with different currents. Torch speed 2 mm/s, 250 mm \times 50 mm \times 3 mm stainless steel plate, arc length 3.5 mm, argon flow-rate 10 l/min, weldment as shown in Fig. 2

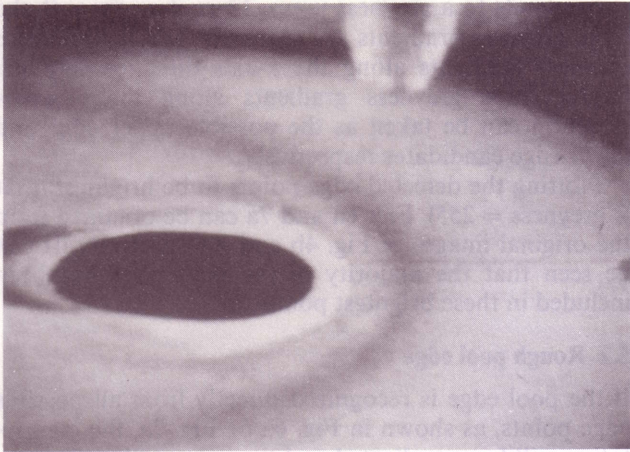
The LaserStrobe vision system consists of a strobe illumination unit (pulse laser), camera head and system controller (6). The pulse duration of the laser is 3 ns. The wavelength is 337 nm in the near-ultraviolet portion of the optical spectrum. The pulse is generated using an extremely fast high-energy electrical discharge through a sealed cavity containing high-purity nitrogen gas. During the laser duration, the intensity of laser illumination is much higher than those of the arc and hot metal. To capture the image during the laser pulse, the camera shutter has been synchronized with the laser pulse. This synchronization is realized through the system controller which sends appropriate trigger commands to fire the strobe unit and initiate the shuttering of the camera head. A narrow-band optical filter has been equipped to match the laser wavelength. Using this vision system, good weld pool contrast can always be obtained for different welding conditions. Quality images can be acquired for the possible real-time pool edge recognition.

The camera is attached to the torch, viewing the weld pool and the surrounding area as shown in Fig. 1. The image coordinate system xy is also shown in Fig. 1, where the x axis and y axis correspond to the bead width and pool length directions respectively. The video signal from the camera is digitized by a frame grabber.

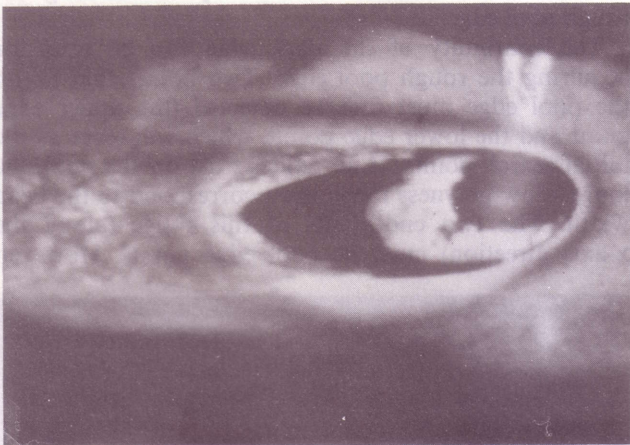
The memory of the frame grabber can be accessed by the computer (486DX66) for image processing. The frame grabber is 512 \times 512 8 bit. The field of view is 20.8 mm \times 14.2 mm. The resolutions along the x and y directions are $\text{pixel}_x = 0.0406$ mm and $\text{pixel}_y = 0.0277$ mm respectively. In most cases, ideal images as shown in Fig. 4a can be acquired by our vision system. However, imperfect images are also sometimes encountered. Some of these imperfect images are shown in Fig. 4b and c. For example, when unmolten oxides or impurities exist, the pool's mirror-like reflectivity will be disturbed, as can be seen in Fig. 4b and c. [The algorithm for the pool width extraction proposed in reference (5) has failed in this case.] Also, the remaining arc effect and complicated pool rear may be encountered. For machine vision, these imperfections will complicate the recognition even though the pool edge can still be easily identified by a human.

4 PERFORMANCE REQUIREMENT

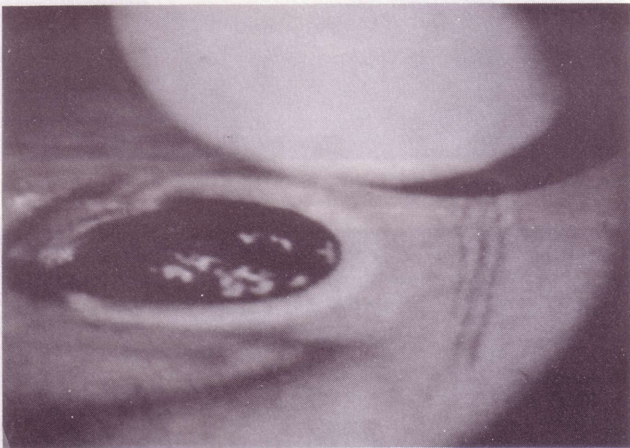
In this study, only the pool recognition problem will be addressed. However, the prospective application is the real-time control of the welding process. Thus, the performance requirement for the pool recognition should be determined according to the real-time control.



(a) Ideal image of dark pool. 120 A current, 6 mm arc length, 3 mm/s torch speed, 250 mm × 100 mm × 3 stainless steel plate, 15 l/min argon flowrate



(b) Oxides existing on the pool diffusely reflect the laser as the solid material does. The remaining arc light makes the pool region also bright. 115 A current, 3.5 mm arc length, 2 mm/s torch speed, 250 mm × 50 mm × 3 stainless steel plate, 10 l/min argon flowrate



(c) Oxides existing on the pool diffusely reflect the laser as the solid material does. The complicated imaging near the pool rear makes the solidified material dark as the pool is. 40 A current, 2.5 mm arc length, 2 mm/s torch speed, 250 mm × 70 mm × 1 stainless steel plate, 8 l/min argon flowrate

Fig. 4 Typical images

Assume that the typical torch speed is about 2 mm per second. To control the welding process, the sampling interval along the seam must be small. If this interval is selected as approximately 1 mm, the corre-

sponding time interval is 500 ms. In this 500 ms interval, the image is first sampled, then converted into video signal and digitized. Once the pool size is obtained based on the image processing result, the control algorithm is implemented to calculate the new welding current. The sampling, that is the optical sensing on the image plane, can be completed instantaneously. However, the scanning of a frame image will take 1000/30 ms. (The digitization into the frame grabber is completed simultaneously in this period.) Also, there is a delay between the sampling command and the actual sampling moment. This delay, which depends on the camera status, may reach a maximum of 1000/30 ms. The implementation of a moderately complex control algorithm usually costs less time compared with the image acquisition and processing. Thus, a machine vision algorithm that can recognize the weld pool edge in 250 ms is required. Such an algorithm can be regarded as real-time.

It will be difficult to quantitatively measure the accuracy of the algorithm. To the authors' knowledge, no other more accurate measuring system for pool geometry is available. Thus, the accuracy will be evaluated through human visual inspection during on-line image processing.

5 IMAGE PROCESSING

Although the LaserStrobe camera provides quality images, the pool edge extraction is still not straightforward, owing to the influences of surface defects, impurities, oxides and material reflectivity. Also, the weld pool size, shape and position may change during welding. Although a human can extract the weld pool edge easily from the images, a machine algorithm cannot do so easily in real-time.

A two-step procedure has been proposed to recognize the pool geometry. In the first step, the image processing is performed to acquire candidate edges which contain the pool edges. The candidate edges are then sorted by a pattern recognition technique to extract the pool edges in the second step, that is the recognition step. To simplify the recognition, obvious non-pool edges have been eliminated from the candidate edges in the image processing step.

This section addresses the image processing step. In this step, all possible edges are detected first. Then, based on the continuity of the pool edge, the rough pool edge and range are determined to eliminate the obvious non-pool edges. The rough pool edge can be segmented at its discontinuities. Since the short segments may not lie on the pool edge, their alternatives are searched to ensure inclusion of all of the pool edge segments in the candidate edges.

5.1 Edge detection

The possible candidates for the pool edge segments must be the edges existing in the image. However, other edges (for example the torch edge, electrode edge and oxide edge) also exist on the images. A direct algorithm could be developed for the pool edge detection, but such an algorithm would not be robust or computation efficient. An algorithm capable of distinguishing the

pool edge from other edges will be more robust and computation efficient.

At a certain y , the image is scanned along the x -axis direction. Once the scanning along the x -axis direction is completed, the y coordinate is increased and the scanning along the x -axis direction is repeated. During the scanning along the x -axis direction, the possible edge points are detected. The scanning procedure is illustrated in Fig. 5.

The pool edge can be divided into two portions, that is the upper and lower sides (see Fig. 5). At the upper edge, the greyness is supposed to sharply decrease along the scanning direction (x -axis) while it increases for the lower side edge. In the ideal case, the greyness of the weld pool is zero. However, the remaining arc effect may exist. In addition to the oxide area, the non-zero greyness can, therefore, also be encountered on the weld pool. Thus, a pure threshold method may not be proper for detection the pool edge.

Before scanning the edge along the x -axis direction, the lowest greyness along the x -axis direction can be determined. This lowest greyness is denoted as $g_{low}(y)$. If no arc effect is encountered during this scanning, $g_{low}(y)$ should be zero. In this case, the pool edge is often accompanied by a sufficient greyness jump. The pool edge can be reliably detected through a thresholding technique. The threshold $T(y)$ can be selected as

$$T(y) = \{\min g + g_{low}(y)\}(1 + \Delta) \quad (1)$$

where Δ is the relative thresholding level and $\min g$ is a small greyness level. The introduction of $\min g$ is to improve the robustness of the thresholding. For example, if $g_{low}(y) = 0$, the threshold $T(y)$ will be zero if no $\min g$ is incorporated. The edge detection performance will be very poor. Due to the large greyness difference between the pool and solid material, the selections of both $\min g$ and Δ are not crucial. From experiments, $\min g$ and Δ have been selected as 5 (greyness level) and 20 per cent respectively. Using the acquired $T(y)$, the possible greyness jump can be detected. If the greyness changes from high to low during scanning along the x -axis direction, the detected edge can be used as the upper edge candidate. If the greyness changes from low to high, the lower side candidate is acquired.

If the arc effect is encountered, $g_{low}(y)$ will not be zero. In this case, the greyness threshold will be difficult to determine due to the variable arc effect (see Fig. 4b and c for the arc effect). However, the pool edge still

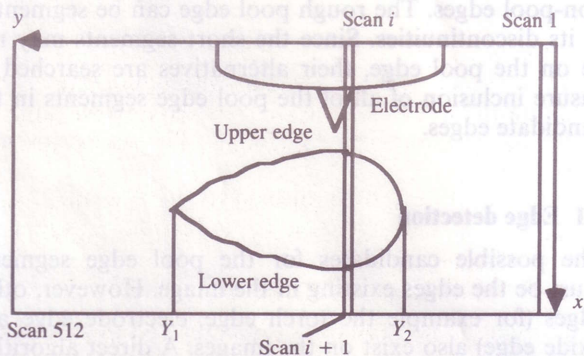


Fig. 5 Edge scanning and edge sides. For a certain y , the image is scanned along the x -axis direction for possible edge points

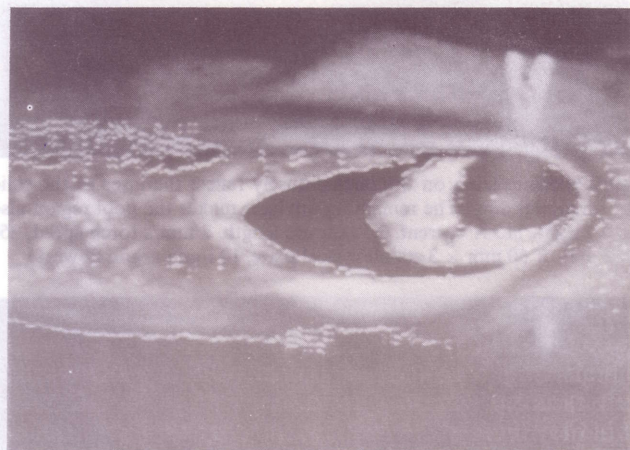
corresponds to a greyness jump. Thus, if $g_{low}(y) > 0$, the large greyness gradients are searched. The largest three greyness gradients along the x -axis direction and the largest three greyness gradients along the $-x$ -axis direction can be taken as the possible upper edge and lower edge candidates respectively.

Plotting the detected edge points to be brightest (that is greyness = 255), Figs 6a and 7a can be obtained from the original images of Fig. 4b and c respectively. It can be seen that the majority of the pool edge has been included in these brightest points.

5.2 Rough pool edge

If the pool edge is recognized directly from all possible edge points, as shown in Fig. 6a or Fig. 7a, the computation will be complicated and time consuming. To simplify the recognition problem, the non-pool edges should be eliminated and the range of interest should be reduced. These will be achieved by determining the rough pool edge.

The continuity of the pool edge can be used for acquiring the rough pool edge. Two points that lie on the pool edge must first be detected (the upper edge point and the lower edge point), which will serve as the initial search points. If no oxides exist on the pool, the longest low-greyness range must correspond to the bead width. The two end-points of this range (along the x -axis direction) must be pool edge points. However,

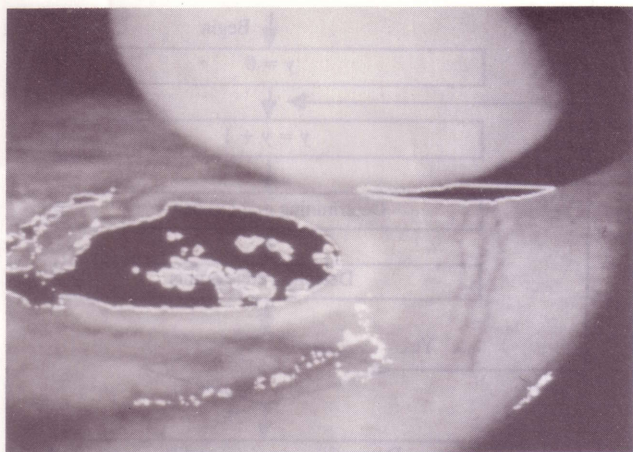


(a) Possible edges

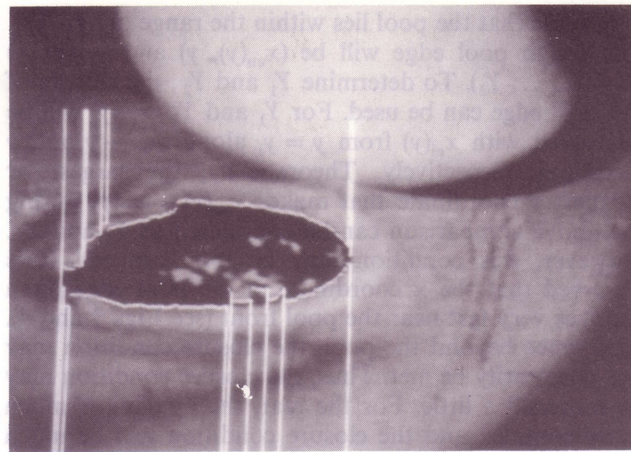


(b) Rough edge

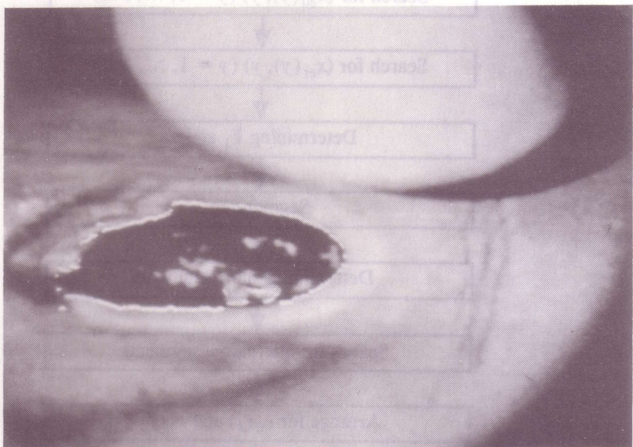
Fig. 6 Possible edges and rough pool edge for image with oxide and arc effect



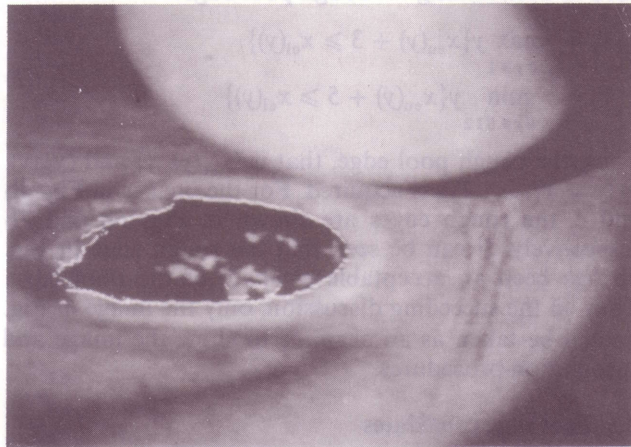
(a) The pool edge is included in the possible edges



(c) Alternatives should be searched for the short segments of the rough pool edge



(b) Non-pool edge is eliminated as much as possible to simplify the recognition



(d) Pool edge candidates include both the rough pool edge segments and their alternatives. The pool edge can be covered by these candidates

Fig. 7 Pool edge recognition procedure

this may not necessarily be true if oxides float on the pool. For example, for the case shown in Fig. 8, two distinct low-greyness regions can be seen which results in two pairs of end-points: (a) the upper pool edge point and the upper oxide edge point and (b) the lower oxide edge point and the lower pool edge point. The longest low-greyness range appears between the upper pool edge and upper oxide edge. In this case, if the continuity is utilized to search for the pool edge with the lower end-point (the upper oxide edge) as the initial search point, the resultant edge will not be the pool edge. Thus, the search continues until only a single pair of end-

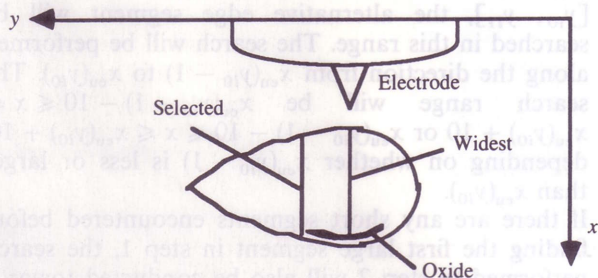


Fig. 8 Initial points for dynamic search. When the oxide is encountered, the upper-lower edge point pairs will be at least two. If no oxide is met, the upper-lower edge point pair may be only one. The largest span from the upper edge to lower edge point may not correspond to the pool upper and lower edge

points are met along the x -axis direction. This pair will be the pool upper and lower edge points and can be taken as the initial search points.

Assume that the upper and lower initial points are (x_{iu}, y_i) and (x_{il}, y_i) respectively. The upper side and lower side edges will be searched separately. For the upper side, the search will be done along both the $-y$ and y directions from (x_{iu}, y_i) . The resultant edge can be denoted as the point set $(x_{eu}(y), y)$ ($y = 1, \dots, 512$). The search can be dynamic, that is searching the new point in the neighbourhood of the last point, because of the continuity of the pool edge. For the search along the y direction for the upper edge, the dynamic search procedure is

1. $x^* = x_{iu}, y^* = y_i$.
2. $y^* = y^* + 1$. Among the possible upper side points along the line $y = y^*$ search for the nearest point (x, y^*) to the point (x^*, y^*) . Denote this nearest point as (x_0, y^*) .
3. If $|x_0 - x^*| > \delta$ (δ is selected to be 20 in this study), let $x^* = x_0$ and $x_{eu}(y^*) = x_0$. Otherwise, $x_{eu}(y^*) = x^*$ and x^* is not changed.
4. If $y^* = 512$, stop. Otherwise, go to step 2.

The search along the $-y$ direction and the lower side search can be completed similarly. Thus, $(x_{eu}(y), y)$ ($y = 1, \dots, 512$) and $(x_{el}(y), y)$ ($y = 1, \dots, 512$) can be obtained.

Assume that the pool lies within the range of $[Y_1, Y_2]$. The rough pool edge will be $(x_{eu}(y), y)$ and $(x_{el}(y), y)$ ($y = Y_1, \dots, Y_2$). To determine Y_1 and Y_2 , the closure of the pool edge can be used. For Y_1 and Y_2 , $x_{eu}(y)$ will be compared with $x_{el}(y)$ from $y = y_i$ along the $-y$ and y directions respectively. Theoretically, the largest or smallest y coordinate that makes $x_{eu}(y) \geq x_{el}(y)$ during the above comparison can be considered as Y_1 and Y_2 . However, this condition may be too stringent. It is observed that the x coordinate of the pool edge often changes very fast near the pool front (see Figs 3 and 4). Also, once beyond the pool, the closure condition may not necessarily be met. Thus, the closure condition may be loosened a little. For the rear, the imaging is much more complex and the closure condition will be much more difficult to meet. To obtain robust estimates of Y_1 and Y_2 , the following closure conditions have been utilized in determining the rough pool edge:

$$Y_1 = \max_{y_i \geq y \geq 1} y \{x_{eu}(y) + 3 \geq x_{el}(y)\} \quad (2)$$

$$Y_2 = \min_{y_i \leq y \leq 512} y \{x_{eu}(y) + 5 \geq x_{el}(y)\}$$

Thus, the rough pool edge, that is $(x_{eu}(y), y)$ and $(x_{el}(y), y)$ ($y = Y_1, \dots, Y_2$), is acquired. For the images in Fig. 4b and c, the rough edges are shown in Figs 6b and 7b respectively. It can be seen that the rough edge in Fig. 6b has been an acceptable estimate of the pool edge. Thus, in the succeeding discussion, only the image in Fig. 4c will be taken as an example to show the image and recognition procedures.

5.3 Pool edge candidates

The rough pool edge is only a preliminary estimate of the pool edge. Non-pool edge segments may still exist. To ensure that the entire pool edge is contained in the final pool edge candidates, the alternatives for possible non-pool edge segments must be acquired. To do this, the rough pool edge will be segmented. Due to the closure associated with the pool edge, short segments should be considered as possible non-pool edge segments and their alternatives will be searched.

The discontinuities of the rough pool edge can be employed for segmenting the rough pool edge. Consider the upper side of the rough pool edge $(x_{eu}(y), y)$ ($y = Y_1, \dots, Y_2$). The difference $d_{eu}(y)$ can be computed as

$$d_{eu}(y) = x_{eu}(y) - x_{eu}(y-1) \quad (3)$$

If the magnitude of the difference is beyond the permitted range, that is

$$|d_{eu}(y)| > d_0 \quad (4)$$

the upper side of the rough edge will be recognized as discontinuous at y , where d_0 is the discontinuity threshold. If d_0 is selected to be too small, too many segments will be generated. The pattern recognition will therefore be complicated. If d_0 is too large, the discontinuities of interest may be missed. From experiments, d_0 is selected to be 5 (pixel). For the lower side, the segmenting can be performed similarly. Thus, the rough pool edge shown in Fig. 7b can be segmented as shown in Fig. 7c.

It has been observed that the rear portion of the pool edge may not be acquired in the rough pool edge in some cases. Thus, the alternatives for the short segments and rear pool edge are required. For the rear of the

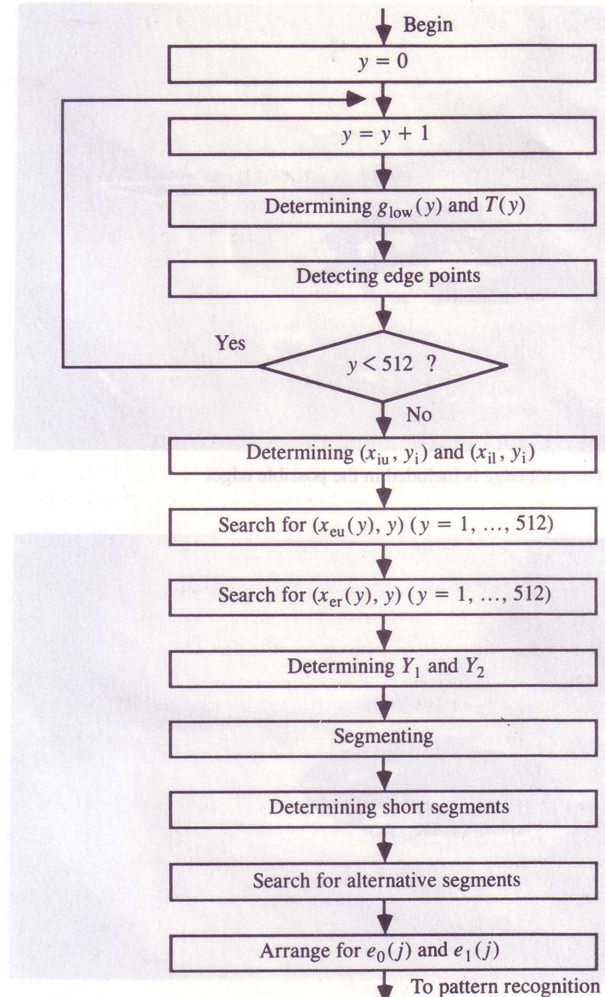


Fig. 9 Flow chart for image processing

pool, the greyness must be zero, except for the oxides, since no remaining arc effect exists there. The range $Y_1^* = Y_2 - (Y_2 - Y_1) \times 0.1 \leq y \leq Y_2^* = Y_2 + (Y_2 - Y_1) \times 0.1$ will be scanned to determine the edge from zero greyness to the non-zero greyness area. The scanning is performed for $x_{eu}(Y_1^*) \leq x \leq x_{el}(Y_2^*)$. For the short segments, the lengths of which are less than 20 pixel, their alternatives can be determined by the following procedure:

1. Scan the segments from the front of the pool to $y = Y_1^*$ until finding a segment longer than 20.
2. Scan the segments towards the rear. When a short segment is encountered, for example in the range $[y_{i0}, y_{i1}]$, the alternative edge segment will be searched in this range. The search will be performed along the direction from $x_{eu}(y_{i0} - 1)$ to $x_{eu}(y_{i0})$. The search range will be $x_{eu}(y_{i0} - 1) - 10 \leq x \leq x_{eu}(y_{i0}) + 10$ or $x_{eu}(y_{i0} - 1) - 10 \leq x \leq x_{eu}(y_{i0}) + 10$, depending on whether $x_{eu}(y_{i0} - 1)$ is less or larger than $x_{eu}(y_{i0})$.
3. If there are any short segments encountered before finding the first large segment in step 1, the search performed in step 2 will also be conducted towards the pool head.

Thus, the alternatives for both the short segments and rear edge can be obtained (see Fig. 7d for the image addressed in Fig. 7). These alternative and rough edge segments provide the final pool edge candidates. For

convenience, the image processing step is summarized in the flow chart of Fig. 9.

6 PATTERN RECOGNITION

It has been observed that the pool edge candidates acquired in the image processing step can always cover the pool edge. The problem is how to select the final segments from all possible segments to construct the pool edge.

Assume that the rough pool edge has been divided into $K - 1$ segments in the range of $[Y_1, Y_1^*]$. The rear portion of the rough edge can be considered as the K th segment. Denote the K segments of the rough pool edge as $e_0(j)$ ($j = 1, \dots, K$). The alternative segments for the short segments and rear edge can be denoted as $e_1(j)$ ($j = 1, \dots, K$), where $e_1(j)$ corresponds to $e_0(j)$ ($j = 1, \dots, K$). Some segments are equivalent for the rough pool edge and its alternative if the corresponding segment length is larger than 20. Assume that there are K_1 short segments. The possible selections for yielding the final pool edge are 2^{K_1} . Suppose that the possible selections are $E^{(i)}$ ($i = 1, \dots, N$), where $N = 2^{K_1}$. A cost function $J(E^{(i)})$ can be optimized to select the best $E^{(i)}$, denoted as $E^{(i^*)}$, utilizing the following criterion:

$$E^{(i^*)}: J(E^{(i^*)}) = \min_{1 \leq i \leq N} J(E^{(i)}) \quad (5)$$

In machine vision, the recognition of regular shapes has been well addressed (16). The recognition of regular shapes or their combination can be fulfilled using standard techniques (17, 18). However, as has been discussed, the weld pool is irregular. To distinguish the pool edge segments from the other edge segments, the inherent characteristics of the pool shape must be acquired and then used to yield the cost function J .

The most obvious feature of the pool edges shape can be characterized by its continuity and closure. Also, the pool edge is smooth. If the pool edge is divided into the four pieces as shown in Fig. 10, C_k ($k = 1, \dots, 4$) may be approximated by the second-order curves. Suppose the corresponding equations are:

$$\begin{aligned} C_1: & y = a_1x^2 + b_1x + c_1 \\ C_2: & x = a_2y^2 + b_2y + c_2 \\ C_3: & y = a_3x^2 + b_3x + c_3 \\ C_4: & x = a_4y^2 + b_4y + c_4 \end{aligned} \quad (6)$$

Principally, if these four models can be fit for different $E^{(i)}$, the corresponding modelling error may be used as

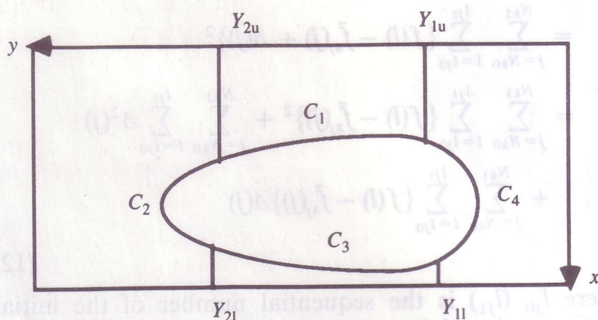


Fig. 10 Pool edge division. The pool edge is divided into four portions. By proper division, the global optimization for the whole pool edge can be decomposed into four local optimizations for the corresponding portions. The computation is drastically decreased

the cost function. However, the corresponding computation will be too large for the real-time algorithm. It can be seen that the second-order derivative associated with any of these four curves should be constant. Thus, the variation of the sampled second-order derivative sequence $\{f(l)\}$ in the curve k , measured by the variance σ_k^2 , should be as small as possible. The fitting degree of $E^{(i)}$ to the second-order curves can then be measured by the following sum:

$$\sum_{k=1}^4 \sigma_k(E^{(i)}) \quad (7)$$

Also, these curves must be connected smoothly. It seems that the joint status of these curves should also be incorporated into the cost function. Thus, in the cost function, both the second-order derivative variation and joint status should be addressed. A proper weight must be selected to compromise these two conditions. The problem is therefore complicated.

To simplify the cost function, the joint condition can be eliminated by means of dividing C_k properly. Take $Y_{1u} = Y_1 + 20$, $Y_{1l} = Y_1 + 20$, $Y_{2u} = Y_1^*$ and $Y_{2l} = Y_1^*$ as the boundaries for C_k (see Fig. 10). If Y_{1u} is not on the boundary of upper edge segments, no $E^{(i)}$ will produce discontinuous joints among C_1 and C_2 . In this case, the respective joint status may not be considered in the cost function. If Y_{1u} crosses the boundary of the upper segments, Y_{1u} can be shifted towards Y_{2u} gradually until the shifted Y_{1u} crosses no boundary of the upper segments. (To reduce the computation, Y_{1u} will be further shifted until a long upper segment is reached. For a long segment, no alternative segment exists and the pool edge in the corresponding range will be this segment.) For other boundaries, a similar adjustment can be done. Thus, the joint conditions can be eliminated from the cost function. The following cost function can be acquired:

$$J(E^{(i)}) = \sum_{k=1}^4 \sigma_k(E^{(i)}) \quad (8)$$

As described, the curve boundaries have been selected on the long segments, crossing no segment boundaries. Thus, for any curve C_k , its two boundary segments have been fixed and have no alternatives. This makes it possible to separate the computations for different σ_k values. The global optimization of equation (5) can be decomposed into four independent local optimizations. Assume that the curve k covers the segments from N_{k0}^{th} to N_{k1}^{th} . The possible selections are $E^{(i)}(k)$ [$i = 1, \dots, N(k)$]. Thus, the following criterion can be used:

$$E^{(i^*)}(k): \sigma_k^2(E^{(i^*)}(k)) = \min_{1 \leq i \leq N(k)} \sigma_k^2(E^{(i)}(k)) \quad (k = 1, \dots, 4) \quad (9)$$

where $E^{(i^*)}(k)$ is the selected C_k and

$$E^{(i^*)} = \bigcup_{k=1}^4 E^{(i^*)}(k) \quad (10)$$

The above decomposition can significantly decrease the computation. Assume that $K_1(k)$ short segments exist in C_k . [It can be shown that $K_1(k) \leq N_{k1} - N_{k0} - 1$.] If the optimization was not decomposed, the cost function in equation (8) would be calculated $2^{\sum_{k=1}^4 K_1(k)}$ times. In the case of decomposition, the cost function

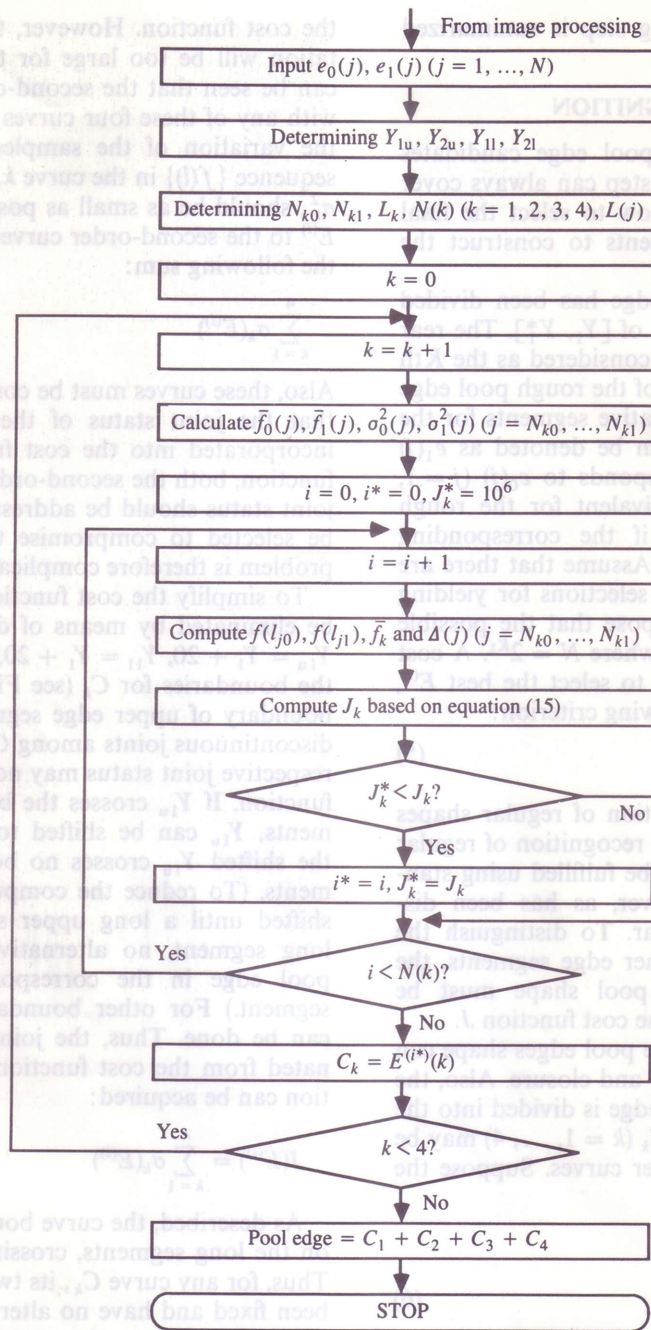


Fig. 11 Flow chart for pattern recognition

for selecting $E^{(i^*)}$ is calculated $2^{K_1(k)}$ times. The computation for the cost function in equation (8) is less than $2^{\max_{1 \leq k \leq 4} K_1(k)}$ times. Let

$$\lambda = \frac{2^{\sum_{k=1}^4 K_1(k)}}{2^{\max_{1 \leq k \leq 4} K_1(k)}} = 2^{\sum_{k=1}^4 K_1(k) - \max_{1 \leq k \leq 4} K_1(k)} \triangleq 2^{K_0} \quad (11)$$

where $K_0 = \sum_{k=1}^4 K_1(k) - \max_{1 \leq k \leq 4} K_1(k)$. Thus, the computation can be decreased by more than $\lambda = 2^{K_0}$ times. If we assume $K_1(1) = K_1(2) = K_1(3) = K_1(4) = 5$, the respective computations for the cost function (8) will be reduced from 1048 576 to only 32.

Consider the curve k . The segments included in this curve range from the N_{k0}^{th} to N_{k1}^{th} . The sample size associated with the segment j is $L(j)$. Denote the segment j as e_{s_j} ($s_j = 0, 1$). It can be seen that s_j depends on $E^{(i)}(k)$. The cost function for selecting the curve k can be calculated through the following equation:

$$\begin{aligned} J_k &\triangleq \sigma_k^2 L_k \\ &= \sum_{j=N_{k0}}^{N_{k1}} \sum_{l=l_{j0}}^{l_{j1}} \{f(l) - \bar{f}_{s_j}(j) + \Delta(j)\}^2 \\ &= \sum_{j=N_{k0}}^{N_{k1}} \sum_{l=l_{j0}}^{l_{j1}} \{f(l) - \bar{f}_{s_j}(j)\}^2 + \sum_{j=N_{k0}}^{N_{k1}} \sum_{l=l_{j0}}^{l_{j1}} \Delta^2(j) \\ &\quad + \sum_{j=N_{k0}}^{N_{k1}} \sum_{l=l_{j0}}^{l_{j1}} \{f(l) - \bar{f}_{s_j}(j)\} \Delta(j) \end{aligned} \quad (12)$$

where l_{j0} (l_{j1}) is the sequential number of the initial (ending) point of the segment j , and

$$\begin{aligned} L_k &= \sum_{j=N_{k0}}^{N_{k1}} L(j) \\ \Delta(j) &= \bar{f}_k - \bar{f}_{s_j}(j) \end{aligned}$$

$$\bar{f}_k = \frac{1}{L_k} \sum_{j=N_{k0}}^{N_{k1}} [\{L(j) - 2\} \bar{f}_{s_j(j)} + \{f(l_{j0}) - \bar{f}_{s_j(j)}\} + \{f(l_{j1}) - \bar{f}_{s_j(j)}\}] \quad (13)$$

where \bar{f}_k is the mean of $\{f(l)\}$ in the whole range of the curve k and $\bar{f}_{s_j(j)}$ is the mean of $\{f(l)\}$ for the interior points of $e_{s_j(j)}$:

$$\bar{f}_{s_j(j)} = \frac{1}{L(j) - 2} \sum_{l=l_{j0}+1}^{l_{j1}-1} f(l) \quad (s_j = 1, 2) \quad (14)$$

It can be shown that

$$\begin{aligned} \sum_{j=N_{k0}}^{N_{k1}} \sum_{l=l_{j0}}^{l_{j1}} \{f(l) - \bar{f}_{s_j(j)}\} \Delta(j) &= \sum_{j=N_{k0}}^{N_{k1}} \{f(l_{j0}) + f(l_{j1}) - 2\bar{f}_{s_j(j)}\} \Delta(j) \\ \sum_{j=N_{k0}}^{N_{k1}} \sum_{l=l_{j0}}^{l_{j1}} \Delta^2(j) &= \sum_{j=N_{k0}}^{N_{k1}} L(j) \Delta^2(j) \quad (15) \\ \sum_{j=N_{k0}}^{N_{k1}} \sum_{l=l_{j0}}^{l_{j1}} \{f(l) - \bar{f}_{s_j(j)}\}^2 &= \sum_{j=N_{k0}}^{N_{k1}} [\{L(j) - 2\} \sigma_{s_j^2(j)}^2 + \{f(l_{j0}) - \bar{f}_{s_j(j)}\}^2 + \{f(l_{j1}) - \bar{f}_{s_j(j)}\}^2] \end{aligned}$$

where

$$\sigma_{s_j^2(j)}^2 = \frac{1}{L(j) - 2} \sum_{l=l_{j0}+1}^{l_{j1}-1} \{f(l) - \bar{f}_{s_j(j)}\}^2 \quad (s_j = 1, 2) \quad (16)$$

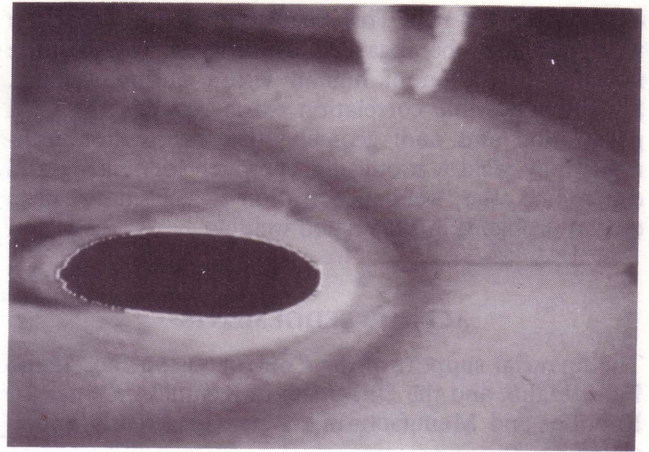
Since $\bar{f}_{s_j(j)}$ and $\sigma_{s_j^2(j)}$ are only required to compute once, the computation for minimizing J_k can be greatly reduced.

It has been shown that the proposed image processing and recognition algorithm can be fulfilled in only 100–150 ms. Thus, a real-time recognition of the weld pool is achieved. The resultant recognition algorithm can be illustrated by the flow chart in Fig. 11.

If the used welding speed and the sampling distance interval along the seam change, the critical image processing speed should be recalculated. A higher welding speed and smaller sampling interval will decrease the sampling period of a control system. The allowed time for the image processing will be decreased. In this study, the image is processed by a PC486DX66 computer. If a powerful multi-processor digital signal processing board is used, the proposed image algorithm may be completed in 30 ms. In the case, the sampling waiting period can be eliminated. The maximum control rate will be 15 Hz. If the maximum sampling distance interval is 2 mm, the allowed welding speed will reach 30 mm per second. The proposed image processing algorithm may be used for real-time control in most GTAW applications.

In addition to being real-time, the proposed algorithm has been shown by extensive experimentation to be accurate and robust against possible welding disturbances. Excellent recognition results are always observed (see Fig. 12 for the recognized pool edges for the typical images).

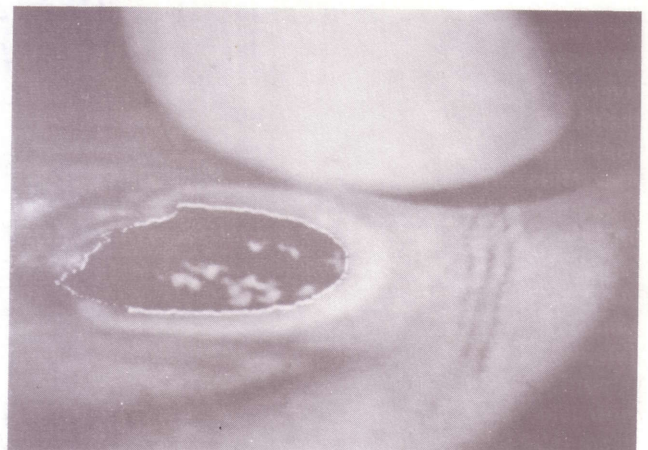
The effectiveness of the proposed image sensing technique has been verified in control practice (19). The extracted pool boundary was used to calculate the area of the weld pool. Using the area feedback, uniform



(a) Ideal images can be easily processed to recognize the pool edge with satisfied accuracy



(b) Satisfied pool edge is acquired despite the oxide and remaining arc effect



(c) Satisfied pool edge is produced by the proposed algorithms even though several oxides and poor rear imaging are encountered

Fig. 12 Recognized pool edges for typical images

welds have been achieved despite the different variations in welding conditions.

7 CONCLUSIONS

Quality images can be acquired by the LaserStrobe camera system. Through the proposed image processing and recognition algorithm, the weld pool geometry can be recognized with sufficient accuracy in real-time

(faster than 150 ms). This precision recognition of the weld pool can be regarded as progress towards the machine emulation of human vision during welding. Since the possible correlation exists between the weld penetration and pool geometry, the recognition technique may yield a promising approach for sensing and controlling the weld penetration which have been crucial problems in automated welding.

ACKNOWLEDGEMENTS

The financial support of the Control Vision Inc., Idaho Falls, Idaho, and the University of Kentucky Center for Robotics and Manufacturing Systems is greatly appreciated.

REFERENCES

- 1 Nagarajan, S., Banerjee, P., Chen, W. H. and Chin, B. A. Control of the welding process using infrared sensors. *IEEE Trans Robotics and Automn*, 1992, **8**(1), 86-93.
- 2 Rokhlin, S. I. and Guu, A. C. A study of arc force, pool depression, and weld penetration during gas tungsten arc welding. *Weld. J.*, 1993, **72**(8), 381s-390s.
- 3 Richardson, R. W., et al. Coaxial arc weld pool viewing for process monitoring and control. *Weld. J.*, 1984, **63**(3), 43-50.
- 4 Brzakovic, D. and Khani, D. T. Weld pool edge detection for automated control of welding. *IEEE Trans. Robotics and Automn*, 1991, **7**(3), 397-403.
- 5 Pietrzak, K. A. and Packer, S. M. Coaxial vision-based weld pool width control. In *Welding and joining processes* (Eds E. Kannatey-Asibu Jr et al.), 1991, pp. 251-264 (American Society of Mechanical Engineers, New York).

- 6 Hoffman, T. Real-time imaging for process control. *Advd Mater. and Processes*, 1991, **140**(3), 37-43.
- 7 Zhang, Y. M., et al. Determining joint penetration in GTAW with vision sensing of weld-face geometry. *Weld. J.*, 1993, **72**(10), 463s-469s.
- 8 Renwick, R. J. and Richardson, R. W. Experimental investigation of GTA weld pool oscillations. *Weld. J.*, 1983, **62**(2), 29s-35s.
- 9 Zacksenhouse, M. and Hardt, D. E. Weld pool impedance identification for size measurement and control. *Trans. ASME, J. Dynamic Systems, Measmt and Control*, 1983, **105**(3), 179-184.
- 10 Tam, A. S. and Hardt, D. E. Weld pool impedance for pool geometry measurement: stationary and nonstationary pools. *Trans. ASME, J. Dynamic Systems, Measmt and Control*, 1989, **111**(4), 545-553.
- 11 Xiao, Y. H. and Ouden, G. den A study of GTA weld pool oscillation. *Weld. J.*, 1990, **69**(8), 298s-293s.
- 12 Yoo, C. D. Effects of weld pool conditions on pool oscillation. PhD dissertation, The Ohio State University, 1990.
- 13 Xiao, Y. H. and Ouden, G. den Weld pool oscillation during GTA welding of mild steel. *Weld. J.*, 1993, **72**(8), 428s-434s.
- 14 Zhang, Y. M., Kovacevic, R. and Wu, L. Closed-loop control of weld penetration using front-face vision sensing. *Proc. Instn Mech. Engrs, Part I*, 1993, **207**(11), 27-34.
- 15 Zhang, Y. M., Kovacevic, R. and Wu, L. Sensitivity of front-face weld geometry in representing the full penetration. *Proc. Instn Mech. Engrs, Part. B*, 1992, **206**(B3), 191-197.
- 16 Davis, E. R. *Machine vision: theory, algorithm, practicalities*, 1990 (Academic Press, New York).
- 17 Dudani, S. A., Breeding, K. J. and McGhee, R. B. Aircraft identification by moment invariants. *IEEE Trans. Computers*, 1977, **26**(1), 39-46.
- 18 Khotanzad, A. and Lu, J. H. Classification of invariant image representations using a neural network. *IEEE Trans. Acoustics, Speech, and Signal Processing*, 1990, **38**(6), 1028-1038.
- 19 Kovacevic, R. and Zhang, Y. M. Model-based predictive control of weld pool area in GTAW. Proceedings of the 1994 American Control Conference, Baltimore, Maryland, 29 June-1 July 1994, pp. 313-317.